

REYNOLDS-STRESS MODELLING OF FLOW AND THERMAL FIELDS IN AN IC-ENGINE-RELATED COOLING CHANNEL

Sebastian Wegt, Maximilian Bopp, Louis Krüger, Suad Jakirlić

Institute of Fluid Mechanics and Aerodynamics

Technical University of Darmstadt

Alarich-Weiss-Str. 10 64287 Darmstadt

wegt@sla.tu-darmstadt.de, jakirlic@sla.tu-darmstadt.de

ABSTRACT

The present work represents an extension of the validation study of a newly developed ω_h -based elliptic-blending-related Reynolds-stress model (EBM) elaborated by Wegt (2021). The EBM formulation has been intensively validated for a multitude of well-known isothermal flow benchmarks involving basic flow scenarios encountered in some canonical fully-developed flow configurations, as e.g. in plane channels and pipes, in developing boundary layers subjected to zero- and adverse-pressure gradients, as well as in flows separating from sharp-edged and curved continuous surfaces, as in flow past periodically arranged hills, over a backward facing step and in differently configured 3D diffusers. The validation study of the EBM formulation in non-isothermal flow conditions is the subject of the present study with the wall impingement of a jet discharging from a fully-developed channel flow serving as a preliminary reference case. This represents the next logical step in approaching the complex flow topology within cooling systems of internal combustion (IC) engines, which is the main goal in relation to the EBM development. Consequently, the non-isothermal analysis is subsequently extended to the so-called WSG ('Water-Spider' Geometry), which represents a generic cooling channel configuration of IC engines. The WSG was designed and developed within the framework of a BMWi project (Klink *et al.* (2021)) and investigated in the framework of isothermal flow simulations by Wegt (2021) and Wegt *et al.* (2022).

INTRODUCTION

The steadily rising requirements for internal combustion (IC) engines imposed by the European union (EU, Heibel (2009) and Gruden (2008)) and the associated manufacturer-related measurements (intelligent thermal management and downsizing, see van Basshuysen (2013) and Lunanova (2009)) cause enhanced thermal loads on IC engines. The cooling system is forced to its failure limit by increased thermal stresses representing subsequently one of the restricting elements within the IC engines and its performance capability. For the best possible design and exploitation of the existing potential of the cooling systems, a test methodology for cooling systems of IC engines as well as for the applied coolants is developed within a complementary experimental and numerical BMWi project (Klink *et al.* (2021)). A part of this intensive cooperation study is the resource-efficient determination of the flow topology within the so-called 'Water Spider Geometry' (WSG). The WSG is designed to serve as a

new reference test sample in relation to the cooling systems of IC engines in practice and is topologically intended to mimic the coolant flow around the cylinder head (see Fig. 8 upper). According to the position of the cylinder chamber in the IC engines relevant to the cylinder head, a one-sided heating of the WSG is experimentally prescribed. This results in a non-uniform heat load on the surface of the WSG leading to a highly complex conjugate heat transfer problem. Apart from the intensive development of an isothermal reference database for the WSG and its constituting flow guiding elements (T-junction, deflections and reverse T-junction), treated in an isolated manner, by a high-fidelity Large Eddy Simulation (LES) within the work of Wegt (2021), a RANS (Reynolds-averaged Navier-Stokes) model formulation, requiring substantially less computer resources for computing the flow field in the WSG, was also proposed on the basis of an elliptic-blending-related Reynolds-stress model (EBM) having the ω_h quantity as the scale-supplying variable. The extensive validation study performed so far was limited to isothermal flow conditions, however the quality of the results obtained supports further efforts towards the extension of the validation study to non-isothermal flow conditions. For this purpose, the perpendicular impingement of a jet originating from a fully-developed channel flow onto a heated wall according to the investigations of Hattori & Nagano (2004) represents a suitable reference case. Finally, the flow in the heated WSG is considered presently in conjunction with the EBM.

COMPUTATIONAL MODEL

The newly developed ω_h -based elliptic-blending-related Reynolds-stress model (EBM) by Wegt (2021) represents a synthesis of the second moment closure (SMC) proposals by Jakirlić & Maduta (2015), Maduta *et al.* (2015) and Manceau & Hanjalić (2002) combining the advantages of the homogeneous dissipation concept and the robust elliptic-blending procedure for the pressure redistribution term. The EBM is implemented in the finite-volume-based, opensource toolbox OpenFOAM[®] and, as previously mentioned, has been validated by computing a variety of isothermal flow configurations. To extend the validation study to non-isothermal flow conditions, the Reynolds-averaged temperature equation

$$\frac{D\bar{\theta}}{Dt} \Rightarrow \frac{\partial \bar{\theta}}{\partial t} + \bar{U}_i \frac{\partial \bar{\theta}}{\partial x_i} = \frac{\partial}{\partial x_i} \left(\frac{\nu}{Pr} \frac{\partial \bar{\theta}}{\partial x_i} - \overline{u_i \theta} \right) \quad (1)$$

is included in the set of governing equations with the mean temperature $\Theta(x_i, t)$, the kinematic viscosity ν and the Prandtl number Pr . Here, the temperature $\bar{\Theta}$ is treated as a passive scalar, implying a negligible temperature dependence on the fluid properties. Within the Reynolds averaging procedure an additional term on the right-hand side of Eq. (1) appeared, denoting the turbulent transport of temperature field and requiring a modeling approach. Thus, the turbulent heat flux $\overline{u_i \theta} = D_{ij} \partial \bar{\Theta} / \partial x_j$ modeled by the gradient approach requires special attention. Presently, the diffusion coefficient D_{ij} is expressed in terms of turbulent viscosity ν_t , but also in terms of the Reynolds stress tensor $\overline{u_i u_j}$.

FLOW IMPINGEMENT

In order to investigate the predictive capabilities of the EBM formulation under thermal flow conditions and with respect to the multitude of flow impingement events within the WSG configuration, the impingement of a jet resembling a fully-developed channel flow with $Re_b = U_b D / \nu = 4560$ onto a partially heated wall and the resulting gap flow toward the outlets are considered in the following. The adopted computational domain is schematically illustrated in Fig. 1, where D denotes the width of the inlet channel, H the height of the outlet gap, and L_H the spatial expansion of the heated area. This flow impingement configuration is based on the detailed DNS study of Hattori & Nagano (2004), whose database serves as a reference for the evaluation of the EBM formulation. The DNS study considers three configurations differing in the gap width H between the partially heated wall and the opposite iso-thermal wall, representing actually the distance between the channel-shaped nozzle and the impinging target, as well as in the spatial expansion of the heated area L_H . All three cases are considered within this validation study; the geometrical details are summarized in Table 1. The partially heated area is subjected to a constant wall heat flux, realized numerically by prescribing a Neumann boundary condition for the temperature equation ($\partial \Theta / \partial y|_{\text{heated wall}} = \dot{q} / \lambda = 1 \text{ K/m}$). The remaining wall segments of the partially heated wall toward the configuration outlets ($|x| > L_H / 2$) and the opposite wall are not heated. The comparatively small temperature gradient on the heated wall allows the temperature to be treated as a passive scalar, allowing the temperature dependence on the flow properties to be neglected. The unclosed turbulent heat flux $\overline{u_i \theta}$ in Eq. (1) is modeled by applying the General-Gradient-Diffusion-Hypothesis (GGDH) with the diffusion coefficient written as $D_{ij} = C_{gg} \overline{u_i u_j} / \omega^h$. The value of the model constant is set to $C_{gg} = 0.3$.

The computational domain illustrated in Fig. 1 is meshed by a two-dimensional, block-structured, fully-hexahedral grid with the OpenFOAM own meshing tool 'blockMesh'. The wall-adjacent cells are clearly positioned within the viscous sub-layer ($y^+ < 1$) to satisfy the low-Reynolds number character of the EBM formulation and to enable the capturing of the boundary layer in its entirety. The grid resolutions used are listed in Table 1 for all three cases. The SIMPLE (Semi-Implicit Method for Pressure Linked Equations) procedure for the pressure-velocity coupling is applied and the discretization for the convective term is done with a second-order upwind scheme. The fully-developed channel flow conditions at the inlet into the flow domain are realized by a separate computation of a channel element by applying the periodic inlet/outlet conditions. The flow thus generated is subsequently mapped onto the domain inlet.

A detailed discussion of the flows structural properties, as

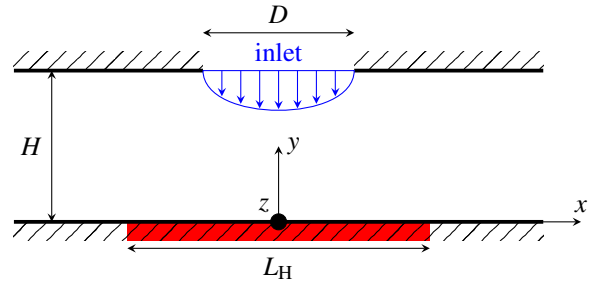


Figure 1. Schematic of the flow impingement configuration with D representing the width of the inlet channel flow, H the height of the outlet gap and L_H the spatial expansion of the heated area. The fully-developed channel inflow is highlighted in blue and the heated area in red.

| | H | L_H | $n_x \times n_y$ |
|--------|---------|--------|------------------|
| Case 1 | $0.5 D$ | $21 D$ | 510×50 |
| Case 2 | $1.0 D$ | $21 D$ | 510×100 |
| Case 3 | $2.0 D$ | $26 D$ | 560×150 |

Table 1. Geometrical details of the three flow impingement configurations according to Hattori & Nagano (2004) and the presently applied grid resolution; n_x and n_y denote the grid cell number in x - and y -directions respectively.

presented in Hattori & Nagano (2004), is omitted here and the focus is set on the predictive capability of the EBM formulation in reproducing the main flow topology. A first impression of the flow topology dependence on the distance H between the channel-shaped nozzle and the bottom wall, characterizing the three flow-impingement cases, is provided in Fig. 2 by illustrating the iso-contours of the velocity magnitude U/U_b (right half) and turbulence kinetic energy k/U_b^2 (left half). The mean flow streamlines originating from the inlet provide a deeper insight into the flow pattern around the stagnation area. The streamline pattern illustrates a severe right-angled skewing of the incoming channel-related flow stream, indicating a strong alternation of flow deceleration and subsequent acceleration in the immediate region around the stagnation point ($x/D = 0$). The incoming perpendicularly-directed flow, featured by a pronounced velocity gradient within this discharging zone, as well as the outflowing wall-bounded jet, resulting from the impingement event, exhibit a clear demarcation from the remaining low-velocity flow region located near the upper wall. Downstream of the impingement region an intense spreading of the wall jet can be observed by the broadening of the streamlines, which is accompanied by the flow relaxation characterizing the post-acceleration region immediately after the impingement occurrence. This relaxation is strongly confined by the presence of the upper wall, which can be especially observed for the Case 1 with the lowest gap height of $H/D = 0.5$ (cf. Table 1). The strongly varying velocity gradient within the shear layer aligned with the streamline dividing the high-velocity flow stream, with respect to both the discharging free jet and the wall-bounded jet, from the weak flow intensity region represents a source of enhanced turbulent activity. This can be clearly seen at the iso-contours of the turbulence kinetic energy in Fig. 2 around and downstream of the sharp edge of the inlet channel. Here, the fast developing free

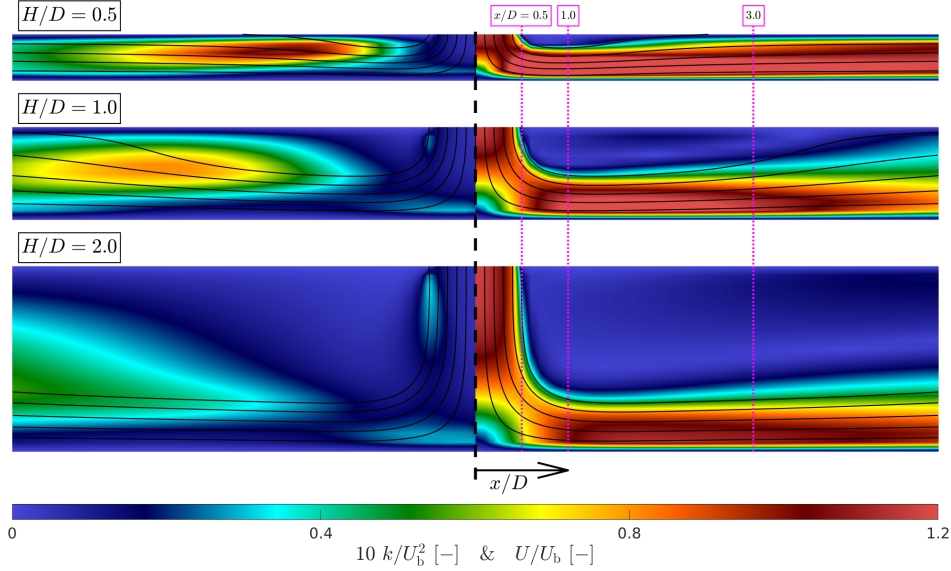


Figure 2. Iso-contours of the turbulence kinetic energy k/U_b^2 (left) and velocity magnitude U/U_b (right) and associated streamlines depicted for the three flow impingement cases considered. The magenta dotted lines mark the line plot positions for Figures 3, 5 and 6.

shear layer between the fully-developed inlet flow and the region of low velocity causes steep changes in the velocity field increasing subsequently turbulence production in this region. The turbulence production is even much more pronounced in the zone bordering the wall-bounded jet and the low-velocity flow region. This wall-jet cross-sectional area extends along the outlet gap, with the outcome being especially pronounced within the Case 1, and represents the location of highest turbulence activity within the flow impingement configuration.

The mean flow topology interpretation allows identification of characteristic flow locations within immediate impingement and wall-jet regions, enabling a more focused assessment and classification of the EBM's predictive performance. For this purpose, the mean flow and turbulence quantity profiles determined with the EBM formulation are compared with the DNS data at three selected cross-sections at $x/D = 0.5, 1.0, 3.0$ downstream the impingement center, denoted by the magenta-dotted lines in Fig.2. The selection of the cross-sectional locations is in accordance with the available DNS data. Since a detailed discussion of the entire flow field is beyond the scope the present (6-page long) manuscript, a representative selection of some essential flow quantities is made with the velocity magnitude U/u_τ ($U = (U_x^2 + U_y^2)^{1/2}$), the wall-normal Reynolds stress intensity $\sqrt{\overline{v'v'}}/u_\tau$ and the temperature Θ . The corresponding line plots are depicted in Figures 3, 5 and 6 in direct comparison with the DNS data.

Fig. 3 shows very good agreement of the EBM-related velocity magnitude profiles with the DNS data for all three configurations considered in three characteristic flow regions, the region of immediate impingement ($x/D = 0.5$), the region representing the transition from flow deceleration due to impingement to the flow acceleration and wall-jet formation ($x/D = 1.0$), and within the developing wall-jet region ($x/D = 3.0$). The velocity profiles exhibit strong gradients in both wall-normal and wall-parallel directions. The differently intensive flow acceleration toward and within the wall-jet region in terms of the nozzle-to-wall distance is obtained in close agreement with the DNS study, apart of some slight departure at $x/D = 3.0$. The strongest relative (in relation to

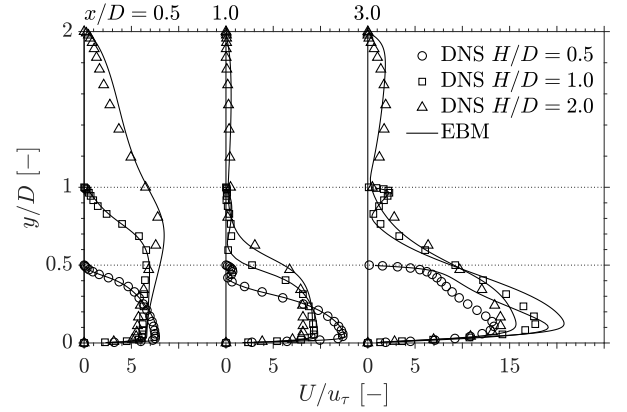


Figure 3. Line plots of the velocity magnitude U normalized by the local friction velocity u_τ depicted at locations $x/D = 0.5, 1.0, 3.0$ (according to Fig. 2). The DNS data of Hattori & Nagano (2004) are represented by symbols.

the U_τ value) acceleration at the last location corresponds, in accordance with the DNS, to the Case 2. Differences observed at the velocity profiles in the immediate wall region are reflected in the friction coefficient distribution (C_f) at the partially heated wall, which is depicted for all three flow configurations in Fig. 4. The EBM results follow closely the DNS data for all three cases concerning both the very strong C_f variation in the immediate impingement region, characterized by a distinct peak, and a flattened C_f development within the far wall-jet region. The deviation far downstream of the impingement is observed for the Case 1 featured by the narrowest gap between the upper plate and lower impingement plate ($H/D = 0.5$) and are directly connected to the characteristic second peak of the friction coefficient development. The EBM is in general capable of reproducing this second peak, but its magnitude is slightly underpredicted and the position is shifted downstream.

The performance assessment of the EBM toward to cap-

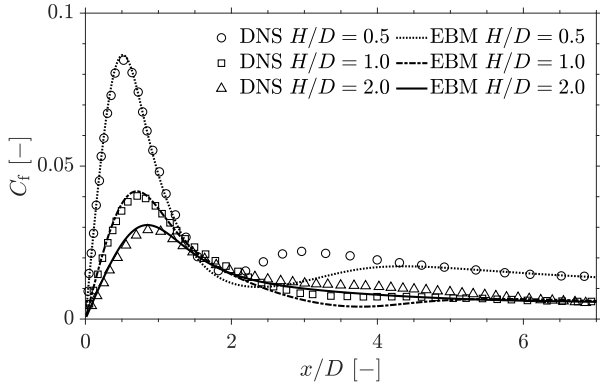


Figure 4. Friction coefficient C_f depicted over x for all three flow impingement configurations. The DNS of Hattori & Nagano (2004) are represented by symbols.

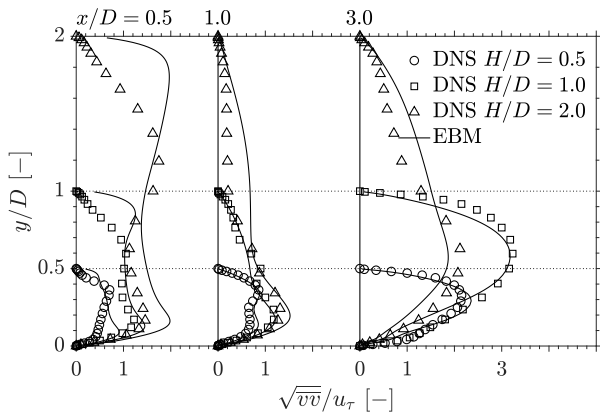


Figure 5. Line plots of the wall-normal Reynolds stress intensity $\sqrt{\overline{v'v'}}$ normalized by the local friction velocity u_τ depicted at locations $x/D = 0.5, 1.0, 3.0$ (according to Fig. 2). The DNS data (symbols) are from Hattori & Nagano (2004).

turing of the turbulence field is presently focused on the wall-normal Reynolds stress intensity $\sqrt{\overline{v'v'}}$ as this is one of the dominant components in the diffusion coefficient in the flow impingement configuration within the so-called gradient approach used for the turbulent heat flux modeling. The corresponding line plots are depicted in Fig. 5. With the exception of the near field of the channel-discharging jet (at $H/D = 0.5$ and $y/D \approx 1.5 - 2$), the EBM returns correctly the reference DNS data over the entire configurations range under consideration. The corresponding EBM-related $\sqrt{\overline{v'v'}}$ profile at $x/D = 0.5$ exhibits a peak value near the top wall that is not reflected in the DNS data. This suggests an overestimation of the turbulent production at the transition of the fully-developed channel flow discharging into the domain (the Reynolds stress distribution within the channel - not shown here for brevity - shows excellent agreement with the respective DNS data).

Finally, the focus is placed on the thermal field that is induced at the partially heated wall. The variations in the temperature field can be observed mainly in the immediate wall vicinity; accordingly, the temperature profiles are depicted within the wall-nearest region in Fig. 6 ($y/D < 0.1$). Starting from the impingement area center, a continuously increased influence of the wall heating on the temperature profile can be observed. This behavior is qualitatively and partially quantitatively correctly reproduced by the EBM, with a somewhat more pro-

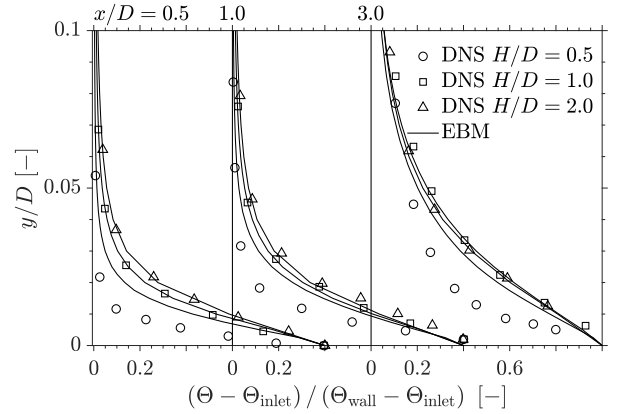


Figure 6. Line plots of the temperature Θ normalized adequately by the inlet Θ_{inlet} and wall temperatures Θ_{wall} depicted at locations $x/D = 0.5, 1.0, 3.0$ (according to Fig. 2). The DNS data (symbols) are from Hattori & Nagano (2004).

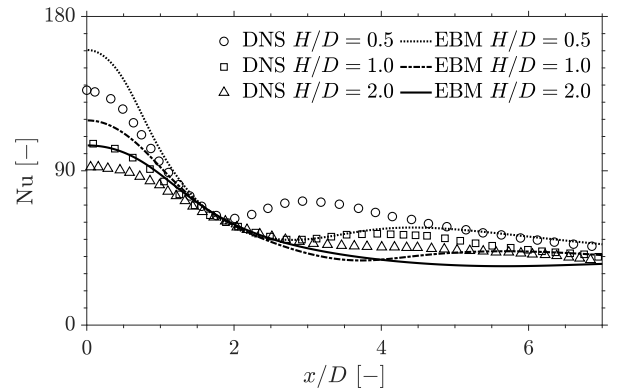


Figure 7. Nusselt number (Nu) distribution over bottom wall for all three flow impingement configurations. The DNS of Hattori & Nagano (2004) are represented by symbols.

nounced departure pertinent to the Case 1 ($H/D = 0.5$). The latter is reflected in a correspondingly enhanced heat propagation into the interior of the flow domain, which is accompanied by a temperature gradient weakening. This is further reflected in the Nusselt number (Nu) distribution at the partially heated wall, depicted for all three cases in Fig. 7. The Nusselt number, correlated directly with the near-wall behavior of the temperature field and its gradient, is reasonably well reproduced by the EBM. Certain deviations are visible in relation to a slight overestimation of the Nusselt number maximum around the impingement center. A well-known characteristics of impingement configurations is the formation of the second Nusselt number peak, the occurrence of which is dependent on nozzle-to-wall distances. Accordingly, it is clearly visible in the Cases 1 and 2, analog to the behavior of the friction coefficient in Fig. 4. This feature represents large challenge for RANS-based turbulence models. In both Cases 1 and 2 the second peak can be indeed observed at the EBM-related results, whereas no peak can be seen in the Nusselt number evolution of the Case 3 in accordance to the DNS study. Although the EBM peaks deviate quantitatively in magnitude and position from the DNS result, their qualitative reproduction in the Cases 1 and 2 can be certainly treated as a reasonably good outcome. This smooth jump at the Nu distribution is, ac-

According to Hadziabdic & Hanjalic (2008, JFM 596), the consequence of a very small detachment of the instantaneous flow field at this location, being beyond the reach of the presently applied steady RANS framework

WATER SPIDER GEOMETRY (WSG)

Following the preliminary computed canonical flow impingement, which demonstrates the potential of the EBM formulation in capturing the thermal flow conditions, the WSG configuration is considered next. We refer to Wegt (2021) and Wegt *et al.* (2022) for more details about the WSG, including geometrical and operating parameters, as well as the comprehensive reference LES study. Here, the double symmetric character of the WSG is exploited and the computational domain is reduced to a quarter, as illustrated in Fig. 8 lower. The inlet conditions corresponds to a fully-developed pipe flow with a bulk Reynolds number of $Re_b = 12600$, which is achieved by a mapping procedure from the pipe inflow immediately downstream onto the WSG inlet. The spatial discretization of the computational domain should ensure a grid-independent solution with the wall-adjacent cells situated completely in the viscous sublayer ($y^+ < 1$). A block-structured fully-hexahedral grid with 1 million cells has been proven to be of sufficient size. For the discretization of the convective term, a blending procedure between the central differencing (CD) and upwind schemes is applied with the CD-fraction of 70 %. To make the convergence procedure more efficient, a pseudo-transient approach is applied. The corresponding temporal terms are discretized with the implicit Euler method.

An intensive discussion about structural flow properties within the WSG would go beyond the scope of the present manuscript. Instead, a brief extraction of the mean flow, turbulence and thermal fields within the $y-z$ -symmetry plane at characteristic locations (see Fig. 8 lower) is exemplary illustrated in Fig. 9 by displaying the profile development of the velocity magnitude U (upper), the streamwise Reynolds stress component $\overline{u'u'}$ (middle) and the mean temperature $[(\Theta - \Theta_{inlet}) / (d \partial \Theta / \partial z)]$. For the turbulence quantity, the root mean square $\sqrt{\overline{u'u'}}$ is presented to account suitably for the significantly different turbulence levels within the WSG and to ensure a meaningful comparison. The corresponding results of the well-resolved, highly comprehensive reference LES according to Wegt (2021) are depicted by symbols.

The flow topology within the WSG is characterized by some typical geometry-driven flow re-directions including flow division (T-junction), deflections and confluence (reverse T-junction), which are closely related to the formation of a dominant vortical topology causing a distinct flow structure. These flow phenomena are the turbulence-driving flow mechanisms, especially related to the localities downstream the T-junction and reverse T-junction contributing substantially to the turbulence level variation within the WSG. These insights are the result of the detailed flow discussion in Wegt (2021). With focus on the predictive capabilities of the EBM formulation, the determination of the velocity field development depicted in Fig. 9 (upper) deserves special attention. The alternation of the velocity magnitude peak as well as its specifically varying behavior within shear layer regions are consistent with the reference LES data. Merely a slight overestimation of the flow magnitude can be seen in the low-velocity region downstream of the inner radius of the T-junction. Furthermore, the highly anisotropic turbulence structure in Fig. 9 middle is a challenging task for RANS-based models, especially with respect to the correct redistribution among the stress compo-

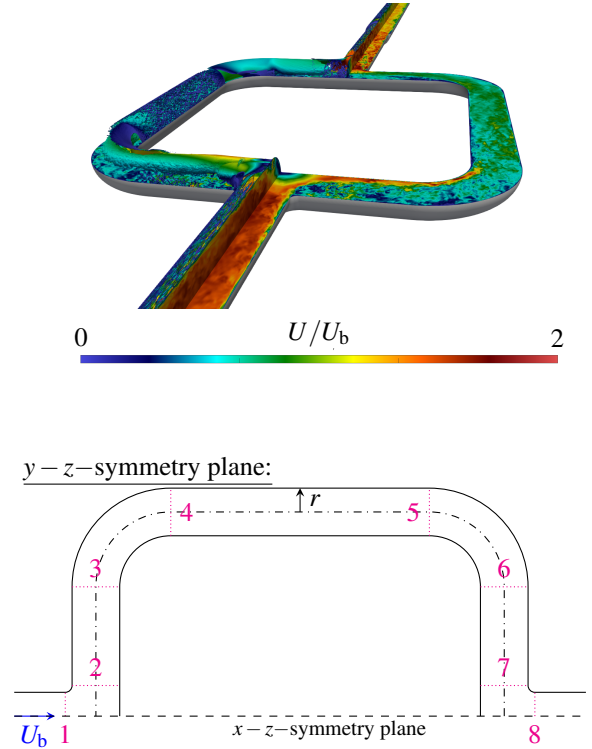


Figure 8. Upper: Instantaneous velocity field visualized by the iso-contours and Q-criterion colored by its magnitude U/U_b ; results originate from the reference Large Eddy Simulation by Wegt (2021). Lower: Schematic of the Water Spider Geometry (WSG) with characteristic locations highlighted by magenta dotted lines (1: T-junction inlet; 2: T-junction outlet; 3: 1. deflection inlet; 4: 1. deflection outlet; 5: 2. deflection inlet; 6: 2. deflection outlet; 7: reverse T-junction inlet; 8: reverse T-junction outlet).

nents. The EBM can inherently cope with the anisotropic character of the turbulence, but tends to slightly underestimate the turbulence level. This can be observed around the emerging shear layer downstream the T-junction and reverse T-junction.

The reproduction of the flow topology by the EBM formulation offers a valuable basis for the analysis of the thermal flow field due to a constantly heated wall with the temperature profiles depicted in Fig. 9 (bottom). In the absence of the thermal reference data, the analysis of the temperature field represents a kind of numerical experiment. The temperature field also exhibits a clearly asymmetric characteristics across the pipe, which varies in the position of its extreme values along the WSG. Here, an inverse response to the position of the velocity peaks in Fig. 9 (upper) can be observed, which can be attributed to a more pronounced convective transport of temperature from the wall into the flow field by a more intense mean flow. The strongest thermal activity within the $y-z$ -symmetry plane occurs in the near-wall region upstream and downstream from the second deflection. Here, the temperature peak shifts from the outer radius at position 5 ($r/R > 0.5$) to the inner radius at position 6 ($r/R < 0$) as a consequence of the flow deflection, which can probably be related to the acting centrifugal forces and the movement of the forming Dean vortices. This brief illustration of the temperature field indicates its structural complexity and gives an impression about the diversity of the flow phenomena interacting within the WSG.

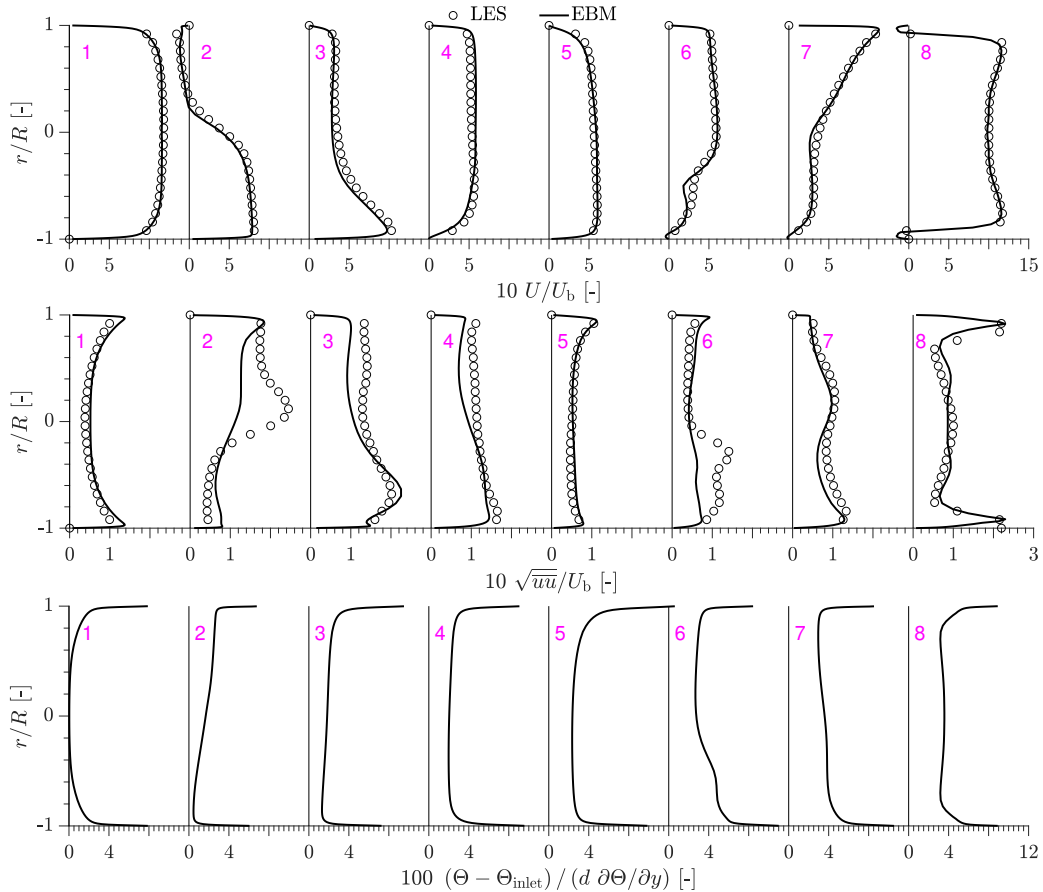


Figure 9. Profile development of the velocity magnitude U/U_b (upper), streamwise Reynolds stress intensity $\sqrt{\overline{u'u'}}/U_b$ (middle) and mean temperature $(\Theta - \Theta_{inlet}) / (d \partial\Theta/\partial y)$ (lower) across the pipe radius r/R at characteristic localities within the WSG according to Fig. 8—lower predicted by EBM (solid lines) and LES (circles).

CONCLUSION

The present validation study has demonstrated the potential of the newly developed Elliptic-Blending Reynolds-stress model of turbulence in reproducing the complex flow topology within the Water Spider Geometry (WSG) under the non-isothermal flow conditions. Preliminary, a generic flow impingement configuration has been computed. The considered flow configurations could be correctly reproduced by the EBM formulation in accordance with the reference DNS and LES studies of Hattori & Nagano (2004) and Wegt (2021), respectively. Some slight deviations, as e.g. in relation to the specific second peak at the Nusselt number distribution, originating mostly from the inherently unsteady character of the underlying turbulence, are addressed to the presently applied steady RANS framework. The thermal field characteristics of the WSG provided by the EBM computations gave an impression of the complex temperature field with changing peaking over the flow pattern and showed the strong coupling with the velocity field..

Acknowledgement Based on a decision taken by the German Bundestag, this project was supported by the Federal Ministry for Economic Affairs and Energy (BMWi) and the AIF (German Federation of Industrial Research Associations eV) within the framework of the industrial collective research (IGF) program (IGF- No.: 20224 N/2). Furthermore, the financial support of the German Research Foundation (DFG) for the Collaborative Research Center/Transregio 150 (SFB-TRR 150, Project Number 237267381) is gratefully acknowledged.

REFERENCES

- van Basshuysen, R. 2013 *Ottomotor mit Direkteinspritzung: Verfahren, Systeme, Entwicklung, Potenzial*. Springer.
- Gruden, D. 2008 *Umweltschutz in der Automobilindustrie*. Vieweg+ Teubner.
- Hattori, H. & Nagano, Y. 2004 *Int. J. Heat and Fluid Flow* **25** (5), 749–758.
- Heibel, M. 2009 *Das wahrgenommene Umweltbewusstsein einer Automarke und dessen Effekt auf die Beziehung zum Verbraucher*. GRIN Verlag.
- Jakirlić, S. & Maduta, R. 2015 *Int. J. Heat and Fluid Flow* **51**, 175–194.
- Klink, A., Wegt, S., Reitz, R., Jakirlic, S., Engler, T., Hussong, J. & Oechsner, M. 2021 Strömungsinduzierte Korrosion und Erosion in Kühlkanälen von Verbrennungskraftmaschinen, IGF-Vorhaben Nr. 20224 N/1 .
- Lunanova, M. 2009 Optimierung von nebenaggregaten. In *Optimierung von Nebenaggregaten*, pp. 93–266. Springer.
- Maduta, R., Jakirlić, S. & Ullrich, M. 2015 In *Turbulence, Heat and Mass Transfer 8*, Hanjalic et al. (Eds.), Begell House Inc., ISBN 978-1-56700-427-4, pp. 299–302.
- Manceau, R. & Hanjalić, K. 2002 *Physics of Fluids* **14** (2), 744–754.
- Wegt, Sebastian 2021 Computational characterization of flow and turbulence in IC engine-relevant cooling channels: An LES- and Reynolds-stress-modeling study. PhD thesis, Technische Universität Darmstadt, Darmstadt.
- Wegt, S., Klink, A., Reitz, R., Hussong, J., Oechsner, M. & Jakirlic, S. 2022 *SAE Technical Paper Series* **2022-01-0394**.